Published in final edited form as:
Phys Med Biol. 2009 March 7; 54(5): 1291–1305. doi:10.1088/0031-9155/54/5/013.

A high sensitivity small animal SPECT system

Gregory S Mitchell and **Simon R Cherry**
Department of Biomedical Engineering, University of California, Davis, One Shields Avenue, Davis, CA 95616, USA

Abstract

Medical imaging using single gamma ray emitting radionuclides typically makes use of parallel hole collimators or pinholes in order to achieve good spatial resolution. However, a tradeoff in sensitivity is inherent in the use of a collimator, and modern preclinical SPECT (single photon emission computed tomography) systems detect a very small fraction of emitted gamma rays, often less than 0.1%. A system for small animal SPECT imaging which uses no collimators could potentially achieve very high sensitivity—several tens of percent—with reasonably sized detectors. This would allow two significant improvements in preclinical studies: images could be obtained more rapidly, allowing higher throughput for screening applications, or for dynamic processes to be observed with very good time resolution; and images could be obtained with less radioactive tracer, making possible the *in vivo* imaging of low-capacity receptor systems, aiding research into new tracer compounds, and reducing the cost and easing the regulatory burden of an experiment. Of course, a system with no collimator will not be able to approach the sub-millimeter spatial resolutions produced by the most advanced pinhole and collimated systems, but a high sensitivity system with resolution of order one centimeter could nonetheless find significant and new use in the many molecular imaging applications which do not require good spatial resolution—for example, screening applications for drug development or new imaging agents. Rather than as an alternative to high resolution SPECT systems, the high sensitivity system is proposed as a radiotracer alternative to optical imaging for small animals. We have developed a prototype system for mouse imaging applications. The scanner consists of two large, thin, closely spaced scintillation detectors. Simulation studies indicate that a FWHM spatial resolution of 7 mm is possible. In an *in vivo* mouse imaging study using the ^{99m}Tc labeled tracer MAG-3, the sensitivity of the system is measured to be 40%. Simple projection images created by analytically combining the two detectors' data show sufficient resolution to observe the dynamic distribution of the radiotracer in the mouse.

1. Introduction

Radionuclide imaging has many applications for molecular imaging in preclinical medical research. In preclinical SPECT imaging system development, the primary emphasis has been almost exclusively in improving spatial resolution (Jaszczak *et al* 1994, Ishizu *et al* 1995, Weber *et al* 1999, Wu *et al* 2000, Meikle *et al* 2001, Acton and Kung 2003, Furenlid *et al* 2004, Beekman *et al* 2005, Madsen 2007)—a sensible and predictable approach given the small size of the imaging subjects' organs. In preclinical SPECT systems and research, pinholes or other collimators are used to form an image of the subject (Meikle *et al* 2005, Loudos *et al* 2003, Bradley *et al* 2006, Beekman and van der Have 2007, Franc *et al* 2008). Many systems have achieved impressive spatial resolution, but this comes with the expense of limited sensitivity (Madsen 2007). Sensitivity is defined for these systems (and this paper) simply as the fraction of emitted gamma rays which are recorded by the system.

gsmitchell@ucdavis.edu.

The sensitivity of small animal SPECT systems is typically 0.1% or lower. There is a direct tradeoff between spatial resolution and sensitivity: smaller pinholes or thicker collimators make for sharper images from better definition of gamma ray trajectories, but this reduces the number of detected events. Physical collimation is not used in small animal PET systems; but due to the physics of 511 keV gamma ray interactions, solid angle coverage, and the requirement of coincidence detection (which functions as electronic collimation), typical system sensitivities are 1-5% (Yang *et al* 2004, Tai and Laforest 2005). With improved sensitivity, *in vivo* preclinical radionuclide molecular imaging studies can be performed with: less time per animal; less radiotracer, which is important for probes with low-yield chemistry or expensive precursors; less dose to investigators performing many scans or to subjects used in longitudinal studies; and better time resolution in dynamic imaging.

Taking the SPECT pinhole (or collimation) sensitivity and resolution tradeoff to one of its limits, with no collimation the achievable system sensitivity becomes essentially determined by two factors: the solid angle covered by the system; and the detection efficiency, including the electronics and data acquisition (DAQ) performance, of its detectors. However, the question then is, can a system with no collimation provide some means of image formation? We believe the answer is yes, though necessarily the image resolution will be poor compared to the submillimeter resolution achieved in some preclinical SPECT systems.

As an aside, in order to set an appropriate comparison and context for the system under consideration here, we briefly discuss optical imaging (Contag and Bachmann 2002, Ntziachristos 2006). Optical imaging used for molecular imaging applications falls into two categories: bioluminescence imaging, which uses either genetically modified cells or mice; and fluorescence imaging, which uses fluorescently labeled molecules and an external excitation source such as a laser. Both of these optical imaging modalities have their attractions, but we note the achievable spatial resolution and ability to reconstruct sources at depth in mice is relatively poor compared to what is routinely the case for radionuclide imaging. For example, the first commercial optical imaging system provided only a single projection view of the animal (Rice *et al* 2001, Troy *et al* 2004). More sophisticated approaches using multispectral images (Kuo *et al* 2007) have demonstrated the ability to reconstruct and localize bioluminescent point sources with millimeter-level precision at depths *in vivo* up to 6 mm, or in homogeneous phantoms at greater depths. But the ability to resolve two point sources at depths of 5 mm or greater is limited to sources separated by 10 mm or more even in homogeneous tissue phantoms (Virostko *et al* 2007). In spite of its spatial resolution and quantitative reconstruction limitations, optical imaging is by far the most commonly used modality for preclinical molecular imaging studies, finding many applications.

Of course choosing the appropriate imaging modality is task-dependent, but for a broad class of preclinical molecular imaging tasks, spatial resolution is essentially unimportant. A SPECT system with relatively low resolution yet very high sensitivity could provide a distinct molecular imaging complement to optical imaging—yielding similar quality images, but making use of an entirely different class of well-developed molecular probes with their associated biochemistry and background properties. One point to make in particular contrast: radionuclide probes are single atom labels, which, compared with large fluorescent labels (molecular weights of hundreds of daltons or more), make for labeling which is less intrusive to the biochemistry of the tracer. Additionally, tomographic reconstruction in optical imaging is an ill-posed inverse problem due to the prevalence of scatter, and this limits both its ability to reconstruct deep sources and its quantitative capabilities. Radionuclide imaging uses more penetrating radiation for imaging and is thus inherently quantitative; the system we consider below holds promise to be quantitative for some applications. We emphasize that there are many applications which do not require good spatial resolution, and a high sensitivity SPECT system will provide an important additional tool for *in vivo* preclinical imaging.

Our system idea, shown in figure 1, consists of two planar, parallel, position sensitive detectors placed close together, with the subject in between. With a close detector spacing, from the resultant good solid angle coverage we expect sensitivity of several tens of percent. For a sufficiently thin imaging subject such as a mouse, simple images can be formed by solid angle effects alone, as we will explain here. First, we note that for a thin continuous scintillator and a position sensitive photomultiplier tube (PSPMT), intrinsic position resolution for detecting a gamma ray interaction is typically, though fairly easily, achieved to be 3 mm FWHM (Weisenberger *et al* 1998,Jeong *et al* 2004). We find from simulation that for a monoenergetic (35 keV) point gamma ray source placed 3 mm away from an uncollimated thin planar detector, the FWHM of the observed interactions on the detector face is 7 mm. This sets the scale for the performance of our system—a point source in a mouse located 3 mm away from a detector will produce a 7 mm diameter spot on the detector (where the size of the spot is defined as the FWHM dimension). Reconstructed resolution is not necessarily limited by the geometry and blurring but these numbers are at least suggestive of the potential scale of image resolution. In addition, some limited resolution in the direction normal to the detector faces is in principle possible: a small source close to one detector will produce a small spot on that detector and a large spot on the opposed detector; a small source in the middle of the two detectors will produce a medium-sized spot on both detectors; and an extended source will produce larger spots on both detectors.

We have developed a prototype system with uncollimated detectors, for high sensitivity small animal imaging. We have performed simulation and reconstruction studies for our system, and used it for a simple proof of concept *in vivo* imaging experiment. Our results are presented in three sections: simulation and reconstruction studies; system construction; and system performance.

2. Simulation and reconstruction studies

We used the GATE simulation software package (Jan *et al* 2004) to study possible system performance. Figure 2 shows a 3D rendering of the simulated geometry: two planar sodium iodide scintillation detectors, each $130 \times 130 \times 3$ mm^3, separated by 22 mm. The approximate size of a prone adult mouse, slightly stretched for imaging purposes, is 90 mm from nose tip to the base of the tail, 35 mm ‘wide’, and 15 mm ‘tall’. Thus a detector separation of 22 mm quite feasibly fits a mouse. In some of the simulation runs described below, for calculating potential sensitivity, between the detectors we placed a 2 cm diameter, 4 cm long water-filled cylinder (to approximate the gamma ray attenuation of a mouse).

We find that for a point source of 140 keV gamma rays (meant to represent ^{99m}Tc) located at the center of the water cylinder, 48% are detected (in total by both detectors), given a definition of detection as 120 keV of deposited energy (or greater) in one of the detectors. We also simulated a monoenergetic 35 keV source (meant to represent the gamma rays from ^{125}I), and for a threshold of 20 keV we find a sensitivity of 68%. For the lower energy source, the water attenuates 15% of the gamma rays. Thus, from simulation of two common SPECT isotopes, we find that very high sensitivity is possible with thin detectors. Thin detectors provide tradeoffs in light spread versus efficiency, so lower energy isotopes are more promising for high sensitivity applications. In small animal imaging, the lower energy gamma rays are not as attenuated and scattered by the animal as they would be in the larger body of a human subject.

In order to assess imaging potential for the system, we placed the simulated lower energy point source at different distances between the detectors, as shown in figure 3. The two figures for each configuration represent the intensity of gamma rays detected at each location on the scintillator face. The FWHM of a profile through the two-dimensional gamma ray distribution in the lower detector (labeled detector 2) changes dramatically as the source is moved closer.

Our planar geometry does not provide sufficiently independent information for a well-posed and unambiguous reconstruction of an arbitrary source distribution. But from combination of the signals of the detectors, we can at least discriminate between point sources at different simulated distances from the detectors, and expect the ability to resolve at the ~1-cm level more complicated source configurations *in vivo*.

From our simulation results, we obtained a series of point spread functions for sources at different depths between the two detectors. Fitting these functions allowed us to produce a parametric form for calculating a complete system matrix **P**, which relates the observed detector data **y** to the distribution of radioactivity **x** as: $\mathbf{y} = \mathbf{P}\mathbf{x}$. Using this system model, we have implemented two reconstruction approaches: a simple ML-EM algorithm assuming **y** is Poisson (Dempster *et al* 1977, Shepp and Vardi 1982, Kay 1997); and finding the singular-value decomposition (SVD) of the matrix **P** in order to directly find an image using the pseudoinverse $\mathbf{P}^+$. We formulated the inverse problem as reconstruction of a volume of five slices, 4 mm thick, each with 21 × 51 2 × 2 mm^2 sized pixels (making 5355 2 × 2 × 4 mm^3 voxels in **x**), using the data obtained in 3 × 3 mm^2 bins of the detector area (41 × 41 bins × 2 detectors = 3362 measurements in **y**).

Convergence of the iterative ML-EM algorithm is accelerated by the choice of initialization: we choose to initialize in our case (for the image **x**) with a volume of $x - y$ slices (uniform in the x and y directions) biased to be 50% larger in the center slice in z (the direction normal to the two detector faces) and less away from the center. A small amount of regularization (using the values of adjacent voxels and a parameter of 1×10^{-7}) via a one-step-late algorithm (Green 1990), helps with reconstruction of deeper point sources in reducing the tendency of the source to be reconstructed at the surface. For the SVD reconstruction, regularization is applied when calculating $\mathbf{P}^+$; the vector of singular values $\mathbf{s} = \{s_i\}$ of **P** is used not simply as the vector of $\{1/s_i\}$ when constructing $\mathbf{P}^+$ from the decomposition of **P**, but as $\{s_i/(s_i^2+\beta_{\mathrm{SVD}})\}$, and we use a value $\beta_{\mathrm{SVD}} = 7 \times 10^{-3}$. Both algorithms are fairly fast to complete, the ML-EM taking less than 10 s per iteration (and run to 50 iterations), and the SVD algorithm essentially instantaneous once the values of the components of $\mathbf{P}^+$ are loaded from a stored file.

To study the performance of our two reconstruction algorithms, we simulated in GATE the response of our system for a cylindrical mouse-sized phantom containing several ^{125}I-like sources (i.e. monoenergetic 35 keV gamma ray sources), as shown in figure 4. The cylinder (8.7 mm radius, 60 mm length) contained 15 kBq of activity as a warm background. The seven additional spherical sources in the simulation were of a size and location consistent with the organs (brain, heart, two kidneys, bladder) and two large xenograft tumors in a real mouse study (Abbey *et al* 2004). Each sphere contained 3 kBq of activity, making for a total of 36 kBq (approximately 1 μCi) in the simulation. The simulation was run to produce 100 s worth of data, or 2.8×10^6 events acquired in the detectors. No noise is included in the simulation (other than statistical, from the number of simulated events in the one realization). The activity concentration ratio of the largest spheres to the cylinder volume is just under 5:1; for the smallest spheres it is approximately 25:1.

Figure 4 shows three projections of the phantom, the true image, the SVD result, and the ML-EM result. The results show that there is ability with our simulated system to quantitatively reconstruct a distribution of sources in a warm background. There is resolution in the z direction (brain and kidneys appear reconstructed in the top slice; heart, bladder, and tumors in the bottom slice), though with a tendency to reconstruct the internal sources with lower intensity and as located more towards the surfaces of the subject. There is also ability to resolve organ systems at the 1 cm level, though (for example) the individual kidneys can't be resolved. Tumors can be seen next to the bladder and kidneys and in the presence of non-specific background if they are bright enough.

3. System construction

For our prototype system, the primary components of the detectors are two large position sensitive photomultiplier tubes (Hamamatsu R3292 PSPMTs). The tubes have a 10 cm diameter active area photocathode, and achieve position sensitivity from 28 × 28 crossed anode wires. The anode wires are read out in a resistive voltage divider circuit which results in four position signal outputs. One of the PMTs is shown in figure 5a.

The PMTs detect events in two thin NaI(Tl) scintillation detectors (St. Gobain). The crystals are 120 mm in diameter, 3 mm thick, and housed in a package with a 250 μm thick Al entrance window and a 2 mm thick optical window. Between the Al entrance window and the scintillator there is a thin piece of low-Z packing material for structural support, and a thin reflector layer. One of the crystals is shown in figure 5b. The detectors were coupled to the PMTs with a small amount of optical grease, and mounted in a plastic housing with foam pieces for support, with each of the two detector assemblies supported by its own simple aluminum frame.

The performance of the lower detector was first tested with two gamma ray sources, ^{241}Am and ^{57}Co, as depicted in figure 6, which shows a flood histogram (with the position of each event determined by an Anger logic algorithm) and an energy spectrum (in analog-to-digital converter, or ADC counts) for the detector, for the two sources placed on the detector face. For this data the center to center separation for the sources was 25 mm. Both sources had an activity of approximately 10 μCi, but the combination of lower branching ratio and a electronic trigger threshold above the iodine escape peak events makes the peak for the ^{241}Am significantly smaller. The FWHM of the ^{241}Am peak (59.5 keV, at 4000 ADC counts) is equivalent to 22% energy resolution, the FWHM of the ^{57}Co peak (122 keV & 136 keV, at 7000 ADC counts) is equivalent to 16% energy resolution. Note the shoulder on the left side of the larger ^{57}Co peak (5000-6000 ADC counts) which is the iodine escape peak in the NaI(Tl) detector. The energy resolution and discrimination of the two sources demonstrates the potential for dual-isotope imaging with the proposed system. The second, upper, detector performs similarly and the two detectors were mounted as shown in figure 7, with electronics as shown in figure 8, to form the complete prototype system. The vertical separation between the active elements of the two detectors was 22 mm (from a physical separation of 16 mm, plus 3 mm on each detector of window thickness/packing material on the crystal housing).

The data acquisition consisted of standard NIM electronics modules, including a shaping amplifier set to a shaping time of 100 ns. The raw signals were combined in a fan-in unit and then a constant fraction discriminator (CFD) was used to produce a logic signal for each of the two detectors. The 14-bit precision DAQ board (UEI PowerDAQ) was triggered if either of the detectors saw an event, i.e. by the logical OR of the CFD signals. Upon a trigger of the board all eight channels were digitized. From the recorded signals, an Anger logic algorithm is used to recover the location of the event in the scintillator.

In order to obtain information to register the detector data with respect to physical location of the imaging subject, glass capillary tubes were filled with ^{99m}Tc in solution. The capillary tubes were placed in a range of horizontal and vertical locations in the system field of view and data acquired for two minutes at each location. A photograph and some detector images are shown in figure 9. (Although the photo shows the upper detector removed, data were acquired with the upper detector in place, and a similar procedure was followed for both detectors.) From this series of images we are able to, by a simple scaling and translation, overlay the detector data on a photograph of the animal subject (though this ignores the nonlinear edge effects of the PMT active area and readout).

4. System performance

The two-detector system was used in an *in vivo* imaging study. In order to demonstrate the potential for dynamic imaging, we selected the ^{99m}Tc labeled radiotracer MAG-3 (obtained from GE Healthcare, Sacramento, CA). MAG-3 is a renal imaging probe and is used clinically to assess kidney function (Maini *et al* 1989). It follows similar biodistribution kinetics in mice (Roberts *et al* 2007), which are to move from the bloodstream to the kidneys to the bladder over the course of several minutes. Two healthy adult (1-year old, approximately 25 g) BALB/c mice were selected for imaging. The mice were imaged for approximately 20 minutes each in the system, with an injected dose of 5.1 μCi for the first scan and 0.75 μCi for the second. The animal study was administered according to the approved animal use protocols of the Center for Molecular and Genomic Imaging at UC Davis.

Each mouse was anesthetized with 2% isoflurane, and anesthesia was maintained during imaging by a nose cone. A piece of thin, absorbent Benchkote paper was placed on the lower detector under the mouse. Mouse body temperature was monitored and maintained by a blown warm air source. A catheter was inserted into the tail vein and a syringe containing a volume of the ^{99m}Tc MAG-3 was prepared. Upon starting the data acquisition, the injection proceeded for 20 seconds. The first mouse injection was carried out with just 5.1 μCi (189 kBq) of the ^{99m}Tc MAG-3. In 12 minutes of data, 53×10^6 events were recorded, corresponding to 7×10^4 cps (counts per second) of OR triggers. The background rate, as measured by data collection with no mouse or radiotracer in the system, was 500 cps total, or 250 cps per detector. The background was measured prior to the imaging scan, and includes events which locate by Anger logic outside of the physical detector area. In the mouse scan data, in addition to removing events outside the detectors, we used an energy cut on the recorded events of approximately 100 keV. Together these cuts eliminate 5% of the data.

Given the low rate of background triggers, we can ignore background for sensitivity calculation. From the trigger rate (70 kcps), cut efficiency (0.95), and activity (189 kBq, including a factor of 0.88 for internal conversion in ^{99m}Tc), we obtain a result of $(70 \times 0.95)/(189 \times 0.88) = 40\%$ sensitivity for *in vivo* use of this isotope and tracer. Modifying our simulation (in section 2) to have round detectors of 85 mm diameter (the size of the useful detector area without edge effects) and using a cut of 100 keV, we obtain a simulation estimate of 47% for our system sensitivity, in reasonable agreement with our system performance.

The images in figure 10 show, in a thresholded display, the geometric mean of the coregistered raw detector data (i.e. of the two projection views) overlaid on a photograph of the mouse, with each frame corresponding to 25 s of data. The series of figures covers the first 6 minutes. The figures thus represent only a fraction (approximately 2 minutes' worth) of the recorded data. The combination of conjugate views in a geometric mean is commonly used in clinical planar imaging quantification (Koral and Zaidi 2006) due to its relatively depth-independent response profile (Cherry *et al* 2003, pp 305-11).

In the first frame of figure 10, three regions of interest (ROIs) are indicated. Plotting the average value over each ROI versus time in figure 11 allows us to see the time dependence of the radiotracer distribution in the mouse. The second ROI is not centered on the animal. The two kidneys in a mouse are not necessarily located at the same depth and our interpretation here is that the images are dominated by events from the kidney closer to the surface.

Figure 12 shows images of a second mouse, which received a 0.75 μCi injection of ^{99m}Tc MAG-3. The data, again in thresholded figures, are frames of a dynamic scan which recorded 22×10^6 events in total. Each frame in the figure represents 5 minutes of data. The time dependence of the biodistribution of the radiotracer in the mouse scans was consistent with other published results (Maini *et al* 1989, Roberts *et al* 2007). We emphasize that this second

scan is a dynamic imaging scan showing biological function in the mouse with less than one μCi of injected tracer compound. We are encouraged by the images we were able to obtain with minimal system calibration, with no reconstruction implemented, and with such a small amount of radiotracer.

5. Conclusion

We feel there is opportunity in preclinical imaging for a radiotracer system with very high sensitivity, and we have constructed a prototype system to demonstrate the feasibility of taking the resolution and sensitivity tradeoff to its limit. This system will be useful for the many imaging tasks which do not require good spatial resolution. For example: rapid screening for drug development, especially in the very common tumor xenograft models (e.g. Hay *et al* 2005); dynamic studies requiring very good time resolution (Celler *et al* 2000); detection, with a high specificity probe, of a small number of cells for a cell trafficking study (Acton and Zhou 2005); or cell-surface receptor studies where the amount of injected radiolabeled molecules is limited by concerns regarding saturation of those receptors (e.g. Zhang *et al* 2006).

Clinical applications for this detector concept (using uncollimated, closely spaced detectors to achieve high sensitivity, and forming images on solid angle effects alone) are limited. One possibility is in extremity imaging, for example to assess response to therapy for rheumatoid arthritis patients. Our system's use is essentially confined to a class of small animal imaging tasks not requiring good spatial resolution, yet benefitting from high sensitivity.

Acknowledgments

This work was supported in part by the UC Davis Academic Federation and by NIH Small Animal Imaging Resource Program (SAIRP) grant U24 CA110804. The authors wish to thank the staff of the Center for Molecular and Genomic Imaging at UC Davis for assistance in carrying out the animal imaging studies. The authors also wish to thank Dr. Yongfeng Yang and Dr. Abhijit Chaudhari for many useful discussions regarding this research.

References

Abbey CK, Borowsky AD, McGoldrick ET, Gregg JP, Maglione JE, Cardiff RD, Cherry SR. In vivo positron-emission tomography imaging of progression and transformation in a mouse model of mammary neoplasia. Proc Natl Acad Sci USA 2004;101:11438–43. [PubMed: 15277673]

Acton PD, Kung HF. Small animal imaging with high resolution single photon emission tomography. Nucl Med Biol 2003;30:889–95. [PubMed: 14698793]

Acton PD, Zhou R. Imaging reporter genes for cell tracking with PET and SPECT. Q J Nucl Med Mol Imag 2005;49:349–60.

Beekman FJ, van der Have F, Vastenhouw B, van der Linden AJA, van Rijk PP, Burbach JPH, Smidt MP. U-SPECT-I: a novel system for submillimeter-resolution tomography with radiolabeled molecules in mice. J Nucl Med 2005;46:1194–200. [PubMed: 16000289]

Beekman FJ, van der Have F. The pinhole: gateway to ultra-high-resolution three-dimensional radionuclide imaging. Eur J Nucl Med Mol Imag 2007;34:151–61.

Bradley EL, Cella J, Majewski S, Popov V, Qian J, Saha MS, Smith MF, Weisenberger AG, Welsh RE. A compact gamma camera for biological imaging. IEEE Trans Nucl Sci 2006;53:59–65.

Celler A, Farncombe T, Bever C, Noll D, Maeght J, Harrop R, Lyster D. Performance of the dynamic single photon emission computed tomography (dSPECT) method for decreasing or increasing activity changes. Phys Med Biol 2000;45:3525–43. [PubMed: 11131182]

Cherry, SR.; Sorenson, JA.; Phelps, ME. Physics in Nuclear Medicine. 3rd. Philadelphia: Saunders; 2003.

Contag CH, Bachmann MH. Advances in *in vivo* bioluminescence imaging of gene expression. Ann Rev Biomed Eng 2002;4:235–60. [PubMed: 12117758]

Dempster AP, Laird NM, Rubin DB. Maximum likelihood from incomplete data via the EM algorithm. J R Stat Soc B 1977;39:1–38.

Franc BL, Acton PD, Mari C, Hasegawa BH. Small-animal SPECT and SPECT/CT: important tools for preclinical investigation. J Nucl Med 2008;49:1651–63. [PubMed: 18794275]

Furenlid LR, Wilson DW, Chen Y, Kim H, Pietraski PJ, Crawford MJ, Barrett HH. FastSPECT II: a second-generation high-resolution dynamic SPECT imager. IEEE Trans Nucl Sci 2004;51:631–5.

Green PJ. Bayesian reconstructions from emission tomography data using a modified EM algorithm. IEEE Trans Med Imag 1990;9:84–93.

Hay RV, Cao B, Skinner RS, Su Y, Zhao P, Gustafson MF, Qian CN, Teh BT, Knudsen BS, Resau JH, Shen S, Waters DJ, Gross MD, Vande Woude GF. Nuclear imaging of Met-expressing human and canine cancer xenografts with radiolabeled monoclonal antibodies (MetSeek™). Clin Cancer Res 2005;11:7064–9.

Ishizu K, Mukai T, Yonekura Y, Pagani M, Fujita T, Magata Y, Nishizawa S, Tamaki N, Shibasaki H, Konishi J. Ultra-high-resolution SPECT system using four pinhole collimators for small animal studies. J Nucl Med 1995;26:2282–9. [PubMed: 8523120]

Jan S, Santin G, Strul D, Staelens S, Assié K, Autret D, Avner S, Barbier R, Bardiès M, Bloomfield PM, Brasse D, Breton V, Bruyndonckx P, Buvat I, Chatziioannou AF, Choi Y, Chung YH, Comtat C, Donnarieix D, Ferrer L, Glick SJ, Groiselle CJ, Guez D, Honore PF, Kerhoas-Cavata S, Kirov AS, Kohli V, Koole M, Krieguer M, van der Laan DJ, Lamare F, Largeron G, Lartizien C, Lazaro D, Maas MC, Maigne L, Mayet F, Melot F, Merheb C, Pennacchio E, Perez J, Pietrzyk U, Rannou FR, Rey M, Schaart DR, Schmidtlein CR, Simon L, Song TY, Vieira JM, Visvikis D, Van de Walle R, Wieërs E, Morel C. GATE: a simulation toolkit for PET and SPECT. Phys Med Biol 2004;49:4543–61. [PubMed: 15552416]

Jaszczak RJ, Li J, Wang H, Zalutsky MR, Coleman RE. Pinhole collimation for ultra-high-resolution small-field-of-view SPECT. Phys Med Biol 1994;39:425–37. [PubMed: 15551591]

Jeong MH, Choi Y, Chung YH, Song TY, Jung JH, Hong KJ, Min BJ, Choe YS, Lee KH, Kim BT. Performance improvement of small gamma camera using NaI(Tl) plate and position sensitive photomultiplier tubes. Phys Med Biol 2004;49:4961–70. [PubMed: 15584530]

Kay J. The EM algorithm in medical imaging. Stat Meth Med Res 1997;6:55–75.

Koral, KF.; Zaidi, H. Methods for planar image quantification. In: Zaidi, H., editor. Quantitative Analysis in Nuclear Medicine Imaging. New York: Springer US; 2006. p. 414-34.

Kuo C, Coquoz O, Troy TL, Xu H, Rice BW. Three-dimensional reconstruction of in vivo bioluminescent sources based on multispectral imaging. J Biomed Opt 2007;12:024007. [PubMed: 17477722]

Loudos GK, Nikita KS, Giokaris ND, Styliaris E, Archimandritis SC, Varvarigou AD, Papanicolas CN, Majewski S, Weisenberger D, Pani R, Scopinaro F, Uzunoglu NK, Maintas D, Stefanis K. A 3D high resolution gamma camera for radiopharmaceutical studies with small animals. Appl Radiat Isot 2003;58:501–8. [PubMed: 12672631]

Madsen MT. Recent advances in SPECT imaging. J Nucl Med 2007;48:661–73. [PubMed: 17401106]

Meikle SR, Fulton RR, Eberl S, Dahlbom M, Wong KP, Fulham MJ. An investigation of coded aperture imaging for small animal SPECT. IEEE Trans Nucl Sci 2001;48:816–21.

Meikle SR, Kench P, Kassiou M, Banati RB. Small animal SPECT and its place in the matrix of molecular imaging technologies. Phys Med Biol 2005;50:R45–R61. [PubMed: 16264248]

Maini CL, Antonacci P, Sargiotto A, Castellano G, Podio V. Dynamic renal scanning using 99mTc-MAG-3 in man. Eur J Nucl Med 1989;15:635–40. [PubMed: 2530091]

Ntziachristos V. Fluorescence molecular imaging. Ann Rev Biomed Eng 2006;8:1–33. [PubMed: 16834550]

Rice, BW.; Cable, MD.; Nelson, MB. J Biomed Opt. Vol. 6. 2001. *In vivo* imaging of light-emitting probes; p. 432-40.

Roberts J, Chen B, Curtis LM, Agarwal A, Sanders PW, Zinn KR. Detection of early changes in renal function using 99mTc-MAG3 imaging in a murine model of ischemia-reperfusion injury. Am J Physiol Ren Physiol 2007;293:F1408–12.

Shepp LA, Vardi Y. Maximum likelihood reconstruction for emission tomography. IEEE Trans Med Imag 1982;1:113–22.

Tai YC, Laforest R. Instrumentation aspects of animal PET 2005. Annu Rev Biomed Eng 2005;7:255–85. [PubMed: 16004572]

Troy T, Jekic-McMullen D, Sambucetti L, Rice B. Quantitative comparison of the sensitivity of detection of fluorescent and bioluminescent reporters in animal models. Mol Imag 2004;3:9–23.

Virostko J, Powers AC, Jansen ED. Validation of luminescent source reconstruction using single-view spectrally resolved bioluminescence images. Appl Opt 2007;46:2540–7. [PubMed: 17429468]

Weber DA, Ivanovic M. Ultra-high-resolution imaging of small animals: implications for preclinical and research studies. J Nucl Cardiol 1999;6:332–44. [PubMed: 10385189]

Weisenberger AG, Kross B, Majewski S, Wojick R, Bradley EL, Saha MS. Design features and performance of a CsI(Na) array based gamma camera for small animal gene research. IEEE Trans Nucl Sci 1998;45:3053–8.

Wu MC, Tang HR, Gao DW, Ido A, O'Connell JW, Hasegawa BH, Dae MW. ECG gated pinhole SPECT in mice with millimeter resolution. IEEE Trans Nucl Sci 2000;47:1218–27.

Yang Y, Tai YC, Siegel S, Newport DF, Bai B, Li Q, Leahy RM, Cherry SR. Optimization and performance evaluation of the microPET II scanner for *in vivo* small-animal imaging. Phys Med Biol 2004;49:2527–45. [PubMed: 15272672]

Zhang X, Xiong Z, Wu Y, Cai W, Tseng JR, Gambhir SS, Chen X. Quantitative PET imaging of tumor integrin $\alpha_v\beta_3$ expression with ^{18}F-FRGD2. J Nucl Med 2006;47:113–21. [PubMed: 16391195]

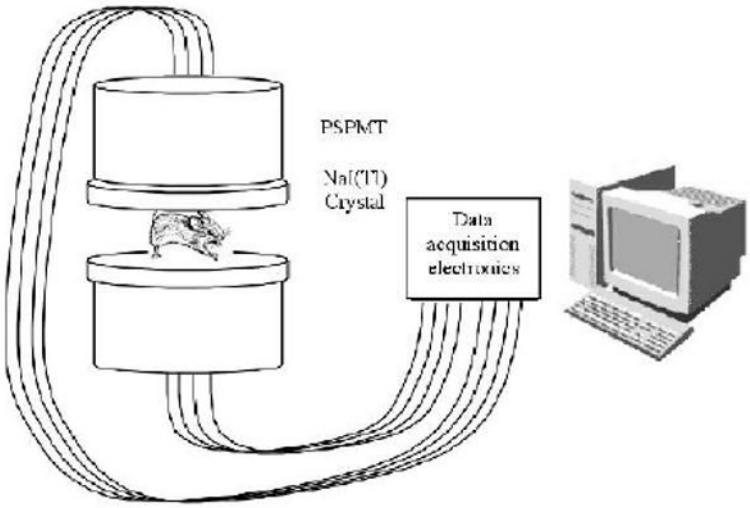

Figure 1.
Conceptual design of a high sensitivity preclinical SPECT system.

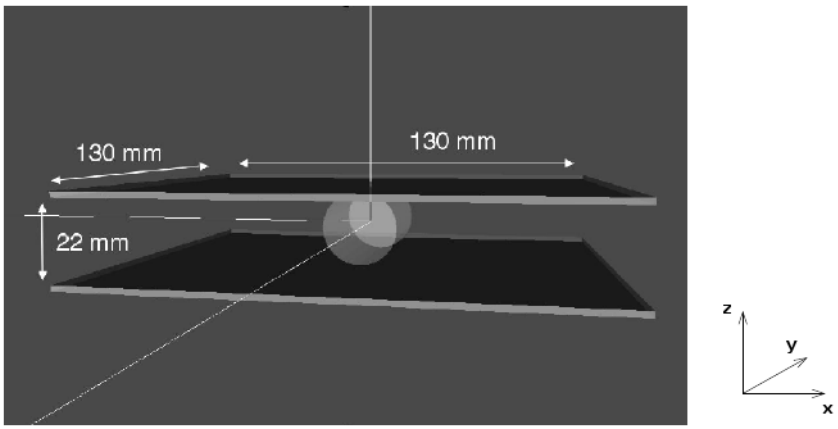

Figure 2.
Rendering of the geometry used for GATE simulations. The detectors are two 3 × 130 × 130 mm^3 NaI(Tl) detectors, with a separation of 22 mm. A 2 cm diameter by 4 cm long water cylinder is used to approximate the attenuation from a mouse. The definition of *x*, *y*, and *z* directions is used throughout this paper.

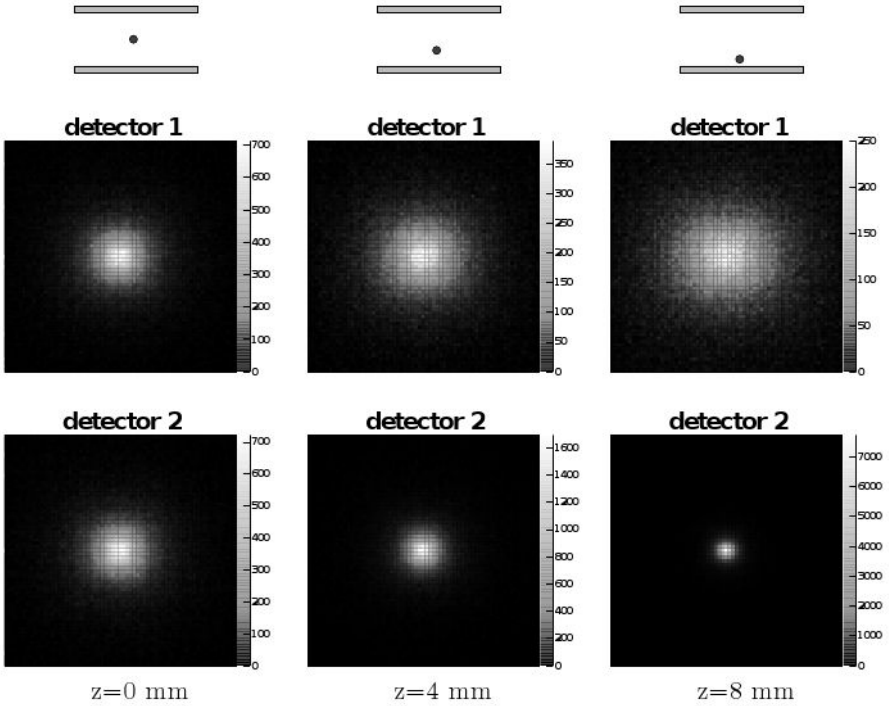

Figure 3.
Simulation results showing the solid angle effect of point source distance from the planar detectors. Three configurations are simulated (left to right); for each the detected gamma ray distribution is shown for the upper (top) and lower (bottom) detector. The color scale represents the number of gamma rays detected on the detector face, white most and black least. Each two-dimensional histogram represents the square detector area with sides of length 130 mm.

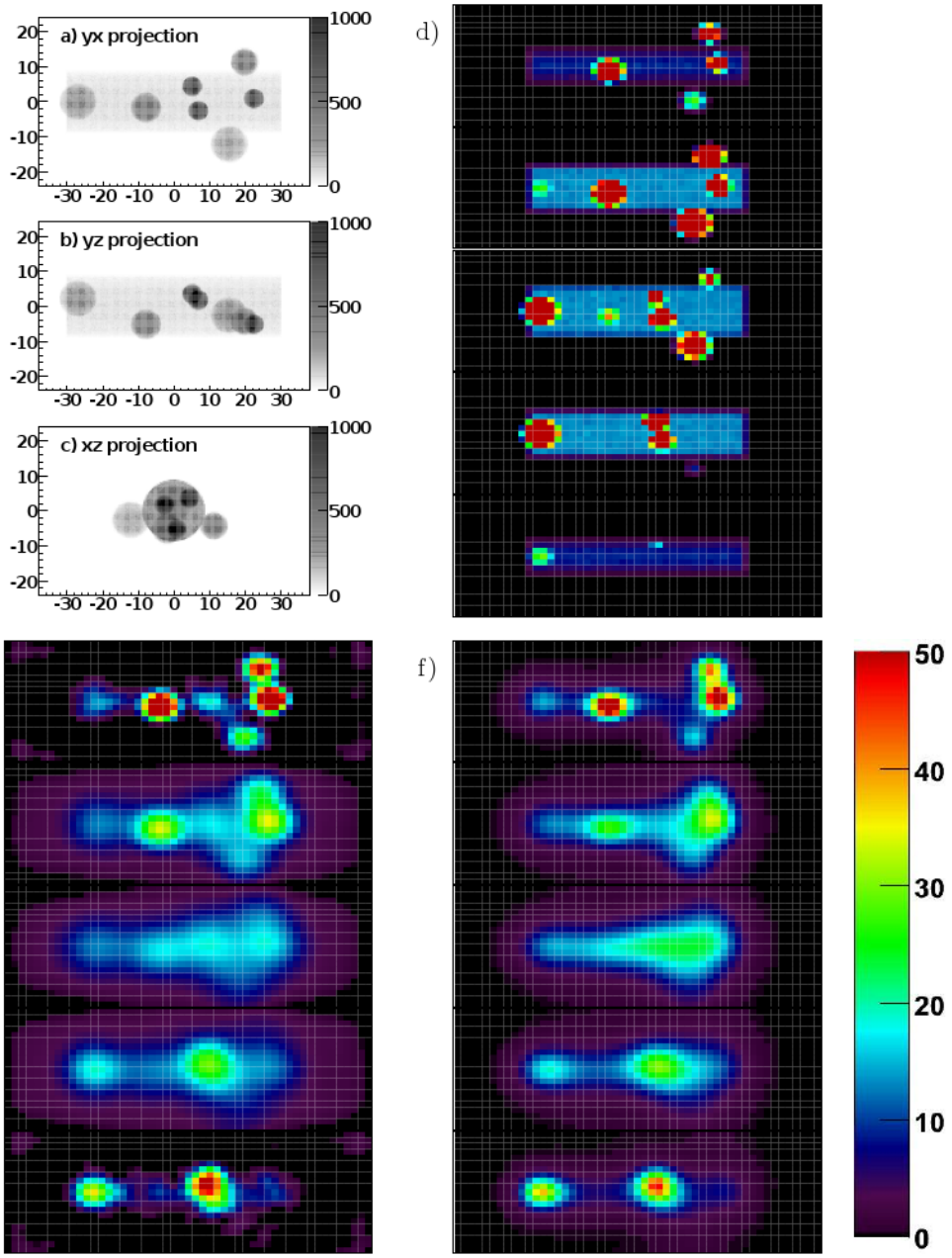

Figure 4.

Image(s) of the true source distribution and reconstruction results for a simulated mouse-sized phantom object with seven internal sources, meant to represent brain, heart, kidneys, bladder, and two xenograft tumors. a), b), and c) are three projection views of the phantom object, with axes labeled in mm and the colorscale indicating the summed intensity of the object in the projection. d) The upper right column of images are the five (bottom to top) slices of the true image, e) the lower left column the corresponding five slices of the SVD reconstruction result, and f) the right column the slices of the ML-EM result. Each pixel in the slice images is 2×2 mm^2, the slices are 4 mm thick. The color scale is for d), e), and f) and units are activity per voxel in Bq.

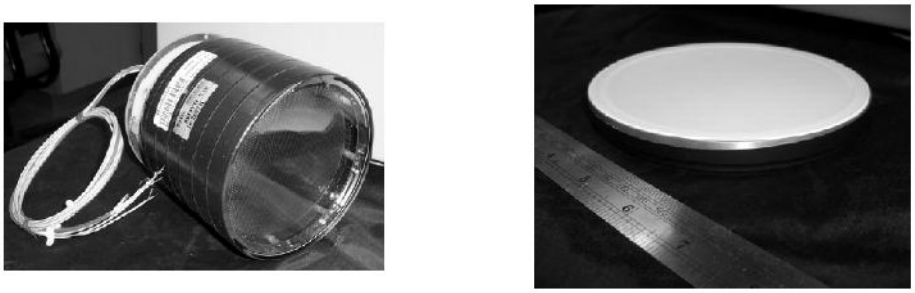

(a) (b)

Figure 5.
(a) Photo of a large PMT (Hamamatsu R3292). (b) Photo of 120 mm diameter NaI(Tl) crystal, 3 mm thick, with a 250 μm aluminum entrance window and a 2 mm thick optical window.

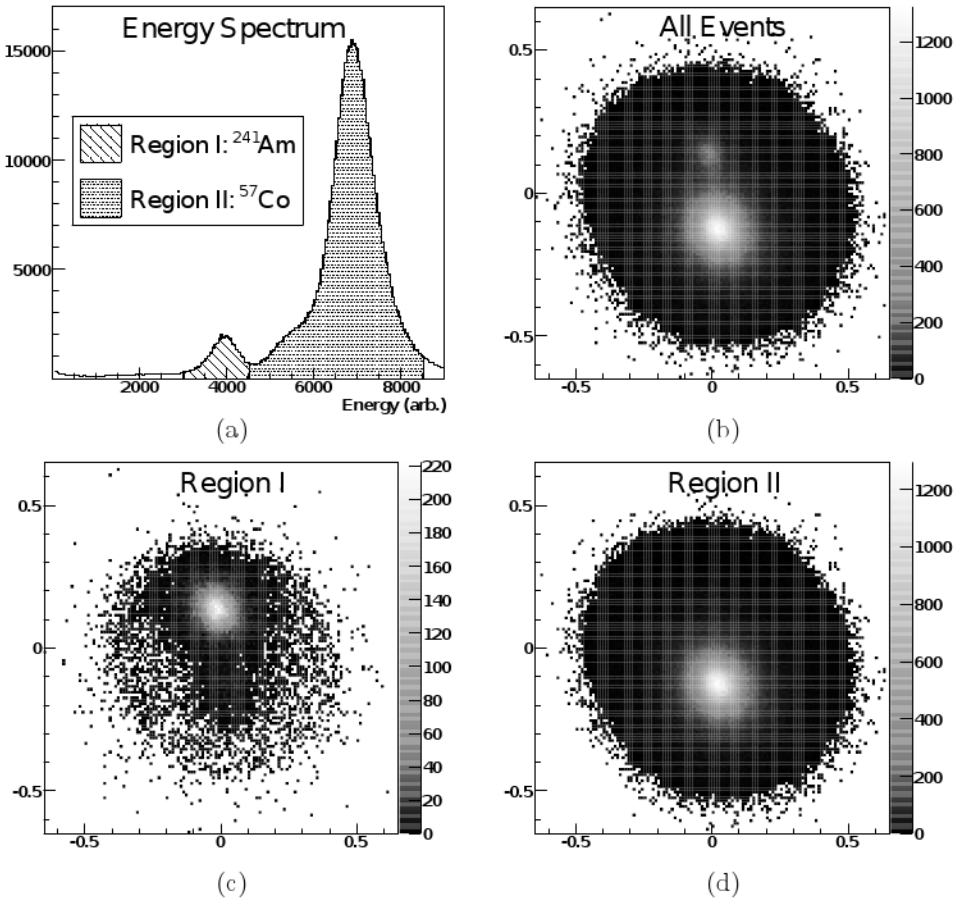

Figure 6.

Energy spectrum and flood histograms under irradiation by two point sources (^{57}Co and ^{241}Am). The upper pair of figures shows (a) the full energy spectrum (sum of the four detector signals) and (b) full flood histogram (produced by Anger logic combination of the four detector signals). (c,d) The two lower plots show subsets of the energy spectrum and the corresponding events positioned on the flood histogram (with different color scale). Note that there is only a hint of the location of the ^{57}Co source in the ^{241}Am energy window in (c), and no sign at all of the ^{241}Am source in the ^{57}Co window in (d).

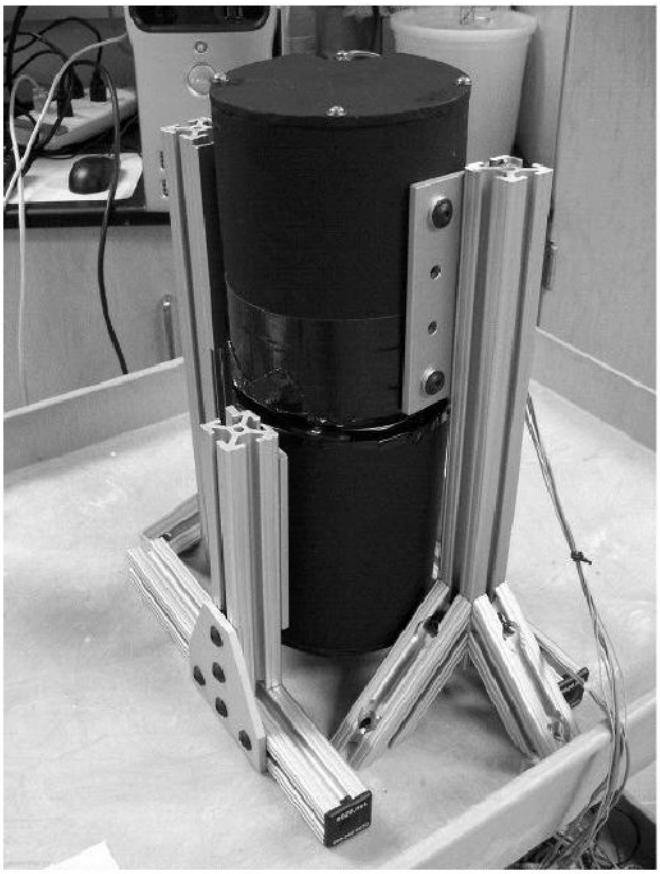

Figure 7.
Assembled prototype system.

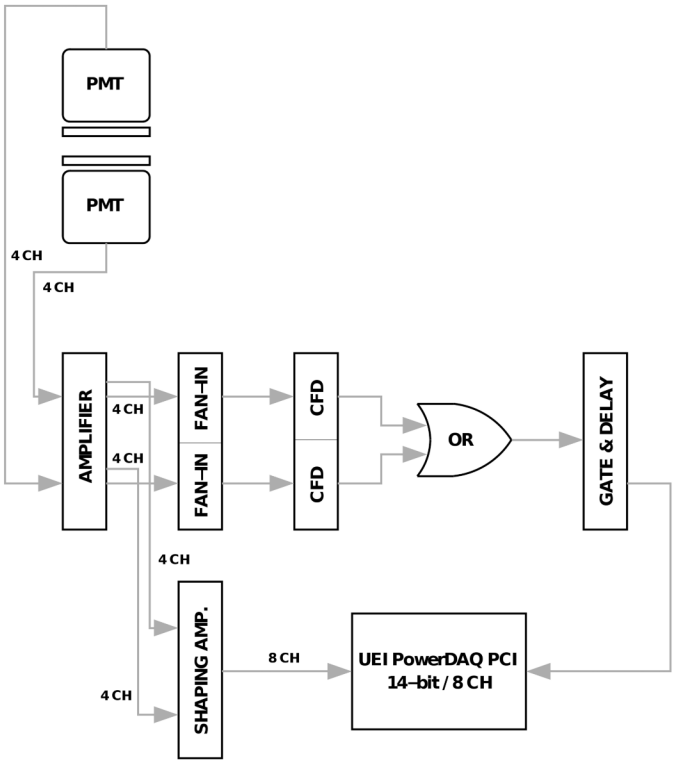

Figure 8.
Schematic of electronics and DAQ for prototype system. The two PMTs have four channels each, for a total of eight channels which are digitized when the sum of either group of four is over a CFD threshold.

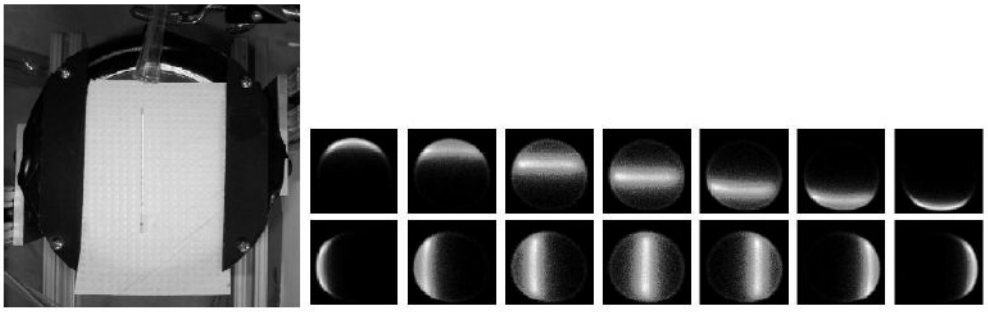

Figure 9.
On the left is a photo of a glass capillary tube on the lower detector, on the right is a series of flood histogram images of the tube at different locations, oriented horizontally in the upper seven plots and vertically in the lower seven. Note the distortion of the signal near the edge of the active area of the detector. The capillary used for these images contained 1.5 μCi of ^{99m}Tc.

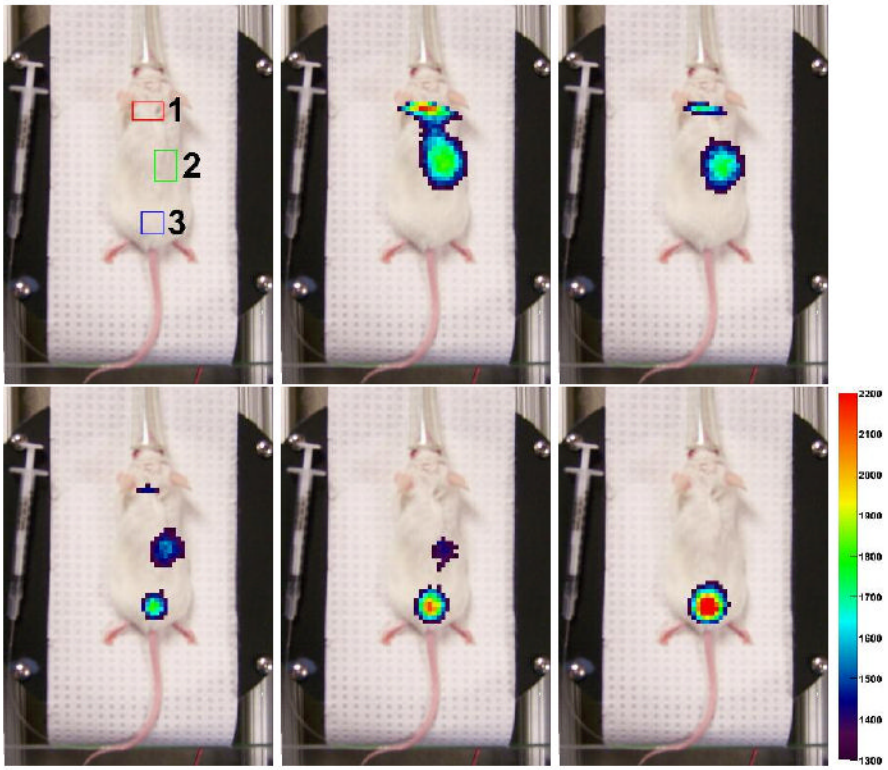

Figure 10.
An indication of three regions of interest, and five frames of a dynamic imaging scan. Each frame represents 25 seconds of data (2×10^6 events), beginning at the times 0, 75, 150, 225, and 300 s after the end of the injection. The pixels from the detector data are a combined (and thresholded) image of the two detector intensities, where the signals are combined by a geometric mean. The combined detector signal shows first a signal from the brain and heart (with detector edge effect artifacts), then signal from the kidneys, and finally a signal only from the bladder. The frames are chosen as one out of every three for the first 6 minutes of imaging. The color scale, which is thresholded, numerically corresponds to the vertical axis of the plot in the following figure 11. The number gives the intensity of the geometric mean of the detectors for that $x - y$ location (2×2 mm^2 bins), in events per 25 s.

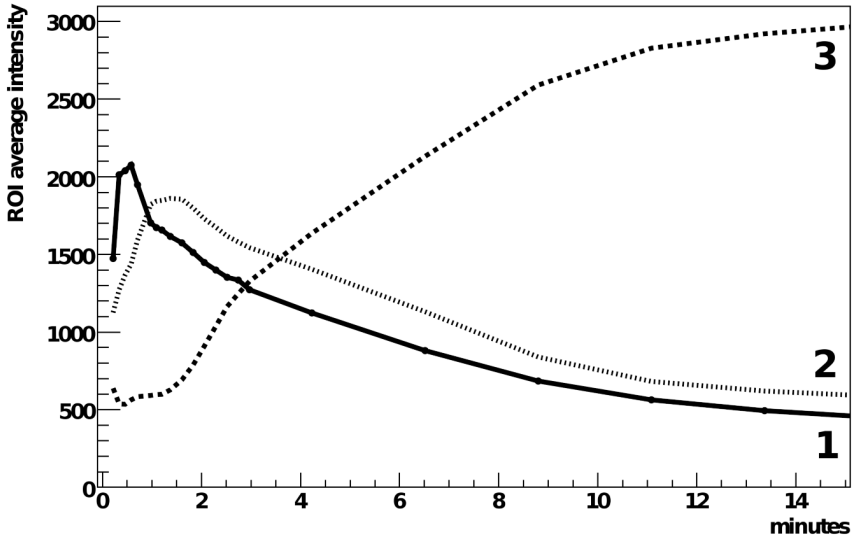

Figure 11.

Time-activity curves for the three regions of interest indicated in figure 10. The units of the ROI average intensity are: events per 2×2 mm^2 area of the detector, averaged over the region of interest, per 25 s (corresponding to 2×10^6 events total in the two detectors), obtained from the (unthresholded) geometric mean combination of the two coregistered detector signals. Note that the scale is identical to the color scale of figure 10.

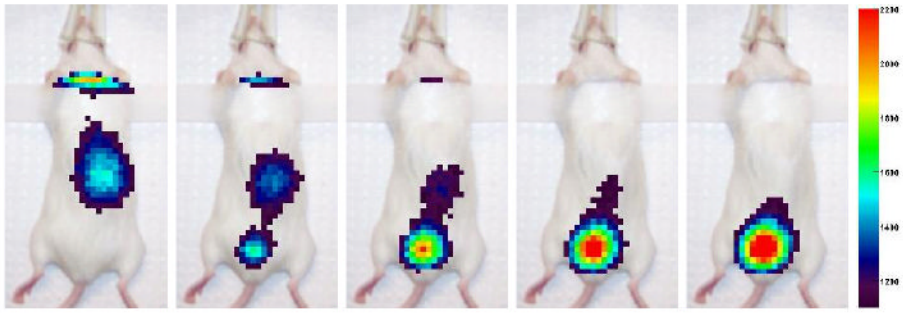

Figure 12.
Five consecutive frames from the second MAG-3 mouse scan, obtained by a procedure identical to figure 10. Each frame across the figure is 150 s of data (2×10^6 events). The total collected data for the whole scan (not all shown) was 22×10^6 events. The scan was performed with injected activity of 0.75 μCi of ^{99m}Tc MAG-3.